Pore types of oil shale in Jilin Province, Northeastern China

Fang Lu[(a–d)], Yan Zhou[(e)], Kexin Jia[(f)], Gang Han[(a)], Ping Wang[(a)]*,
Rui Liu[(g)]*

[(a)]   Hainan Tropical Ocean University, Sanya 572022, P. R. China
[(b)]   Key Laboratory of Island Tourism Resource Data Mining and Monitoring,
    Ministry of Culture and Tourism, Sanya 572022, P. R. China
[(c)]   Hainan Cruise Yacht Research Base, Sanya 572022, P. R. China
[(d)]   Hainan International Island Tourism Research Base, Sanya 572022, P. R. China
[(e)]   Research Institute of Exploration and Development, PetroChina Huabei Oilfield
    Company, Renqiu 062552, P. R. China
[(f)]   Research Institute of Exploration and Development, PetroChina Jilin Oilfield
    Company, Songyuan 138001, P. R. China
[(g)]   Changchun Institute of Technology, Changchun 130021, P. R. China

Abstract. *To better understand and characterize pores in oil shale systems,
samples from four significant oil shale-bearing formations of the Songliao,
Huadian and Luozigou basins in Jilin Province, Northeastern China, namely
Qingshankou (QSK), Nenjiang (NJ), Fengtai (FT) and Longteng (LT), were
prepared by breaking fresh surfaces and argon (Ar) ion polishing both
perpendicular and parallel to bedding and imaged using a field emission
scanning electron microscope (FE-SEM). Interparticle (interP), intraparticle
(intraP) and organic matter (OM) pores are the three types of pores between
or within particles of oil shale, i.e., fossils, minerals and OM. All four samples
contain interP and intraP pores, but only minor OM pores occur in sample QSK.
Sample FT has significant amounts of intrafossil and dissolution (intraparticle)
pores due to the abundance of microfossils and the dissolution possibly caused
by OM decarboxylation. Sample NJ has the highest pyrite content and contains
the greatest amount of pyrite intercrystalline (intraparticle) pores, differently
from sample QSK, whose amount of these pores is the lowest. Sample LT enriched
with clastic particles has a large number of intercrystalline (interparticle)
pores. These pores are primarily at micro- to nano-scales with various shapes,
from irregular to elongated to triangular to polyhedral to rounded to elliptical,
etc. There are differences in the contents of particles and OM pores between oil
shales in Jilin Province and gas shales in North America. The reasons for these
differences may be due to the diverse sedimentary environments and levels of
maturity of oil shales. Besides, high-resolution scanning electron microscope
imaging can be used to describe the diagenetic processes of oil shale.*

* Corresponding authors: e-mails *wpalong@hntou.edu.cn; gglr984@sohu.com*

1. Introduction

The proven reserves of oil shale in Jilin Province are 108.6×10^9 tons, taking the leading place in China. Oil shales are mainly distributed in the Songliao Basin, while the rest are found in the Huadian, Luozigou and other small basins [1] (Fig. 1). Although oil shales in the Songliao Basin cannot be open-pit mined because they are buried in high-yield farmland, nevertheless, these have been successfully exploited by underground in-situ mining technology since 2015. The oil shales in the Huadian and Luozigou basins have been utilized and developed for many years by surface retorting technology, so it is necessary to precisely evaluate the potential of recoverable resources. Pores play an important role in the precise evaluation of unconventional hydrocarbon resources such as oil shale [2–4]. In addition, the type, shape and distribution of pores within oil shale will directly affect its structure integrity and percolation properties which are relevant to the selection of in-situ conversion methods, well spacing, wellbore stability and deliverability [5]. Pore characterization is also important for understanding fluid-rock interactions to reduce the impact of in-situ oil shale conversion on the subsurface environment [6].
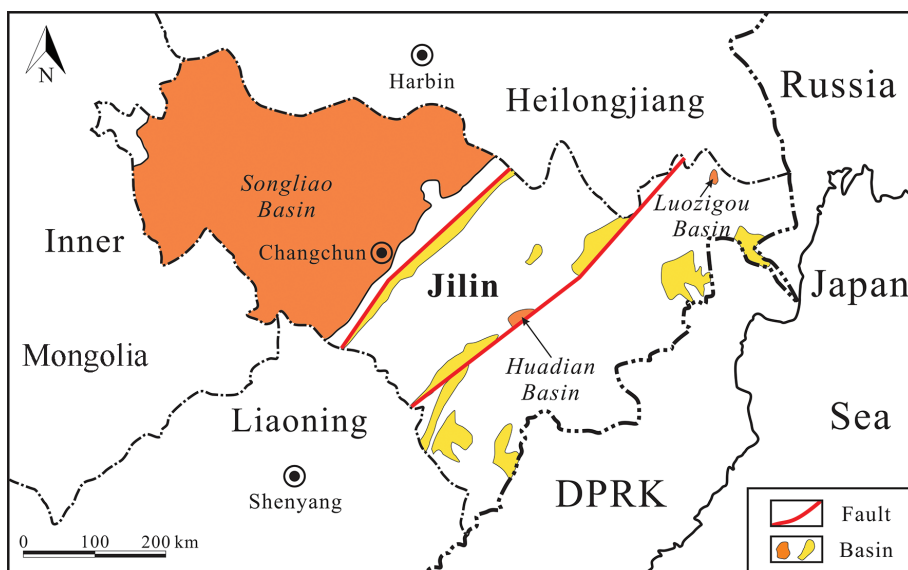

Fig. 1. Simplified geological map and sampling areas in Jilin Province, Northeastern China (modified from [1]).

To date, most studies on the characterization of pores within oil shale have only focused on pore evolution during pyrolysis and have not investigated the parameters of the pores within raw oil shale, such as size, shape and type, by using the scanning electron microscopy (SEM) imaging technique [7–14]. Moreover, all the studies reviewed so far suffer from the fact that it is difficult to obtain high-resolution images for more accurate observation due to the performances of experimental apparatus (e.g., SEM, microtomography (micro-CT)) and conventional sample preparation technique because most pores within mudrock, including mudstones and shales, are smaller than 1 μm [15]. Over the last decade, unconventional reservoirs represented by gas shale have become increasingly prominent in oil and gas exploration. Thanks to the application of argon (Ar) ion polishing and field-emission (FE) SEM techniques, the pore characterization within gas shale gained significant improvement for a better understanding of shale gas production [15–21]. In addition to eliminating pull-out and other artifacts brought by traditional sample preparation for providing flatter observation surfaces, these techniques can produce nanoscale photomicrographs at high resolution more conveniently and economically than other imaging techniques such as focused ion beam-scanning electron microscopy (FIB-SEM), transmission electron microscopy (TEM), atomic force microscopy (AFM), etc. Although gas shale and oil shale are both unconventional mudrock reservoirs, their genesis and composition are quite different, so it is necessary to strengthen the independent investigation of pores within oil shale.

In this work, we investigate the shape, size, distribution and types of pores within raw oil shale samples from three representative basins in Jilin Province: the Huadian Basin, the Songliao Basin and the Luozigou Basin. More specifically, the samples originated from four formations of the abovementioned basins. For the study, the Ar ion polishing and FE-SEM imaging techniques were used. Such observations are crucial in both open-pit mining and in-situ conversion of oil shales. It is shown that Ar ion polishing and FE-SEM imaging are competent techniques for investigating the pore structure of oil shale.

2. Geological setting

Oil shale samples used in this work were collected from the basins of Huadian, Songliao and Luozigou in Jilin Province, Northeastern China (Table 1).

2.1. Huadian Basin

The Huadian Basin is located in Huadian City, southeastern Jilin Province, with an exposed area of approximately 800 km^2 (Fig. 1). It is a Cenozoic nonmarine strike-slip basin developed along the Dunhua-Mishan Fault Zone,

Table 1. Oil shale samples used in the study

Sample ID	Age	Unit name	Location	Sampling coordinates	Basin type	Sedimentary environment	Oil yield, wt% [1, 22]
FT	Eocene	$E_{2\text{-}3}h^2$	Huadian Basin	42°59'49.9"N, 126°51'51.6"E	Strike-slip	Lacustrine	8.59 (avg.), 24.80 (max)
NJ	Late Cretaceous	$K_2n^{1\text{-}2}$	Songliao Basin	44°31'31.6"N, 124°42'15.3"E	Extensional	Lacustrine	3.51–12.10
QSK		K_2qn^1		44°51'3.8"N, 125°35'50.7"E			3.51–9.31
LT	Early Cretaceous	K_1dl^2	Luozigou Basin	43°44'42.0"N, 130°18'22.8"E	Extensional	Fluvial-lacustrine	6.72 (avg.), 14.37 (max)

Abbreviations: FT = Fengtai; NJ = Nenjiang; QSK = Qingshankou; LT = Longteng.

which belongs to the northern extension of the Tancheng-Lujiang Fault Zone [1]. During the deposition of the Huadian Formation ($E_{2\text{-}3}h$), the basin was in the semi-deep to the deep lacustrine sedimentary environment. $E_{2\text{-}3}h$ includes, from bottom to top, the Lower Pyrite Member ($E_{2\text{-}3}h^1$), the Middle Oil Shale Member ($E_{2\text{-}3}h^2$) and the Upper Carbonaceous Shale (coal-bearing) Member ($E_{2\text{-}3}h^3$). $E_{2\text{-}3}h^2$ consists of 6–13 layers of gray-brown or gray-black recoverable oil shale, which are rich in algae fossils. The oil shale has the maximum oil yield at 24.80 wt%, with averages at 8.59 wt% [1, 22, 23].

2.2. Songliao Basin

The Songliao Basin is China's largest and most productive oil-bearing nonmarine basin, it is also the largest oil shale reservoir in the country [1, 23, 24]. The total coverage area of this basin is 260,000 km², of which about 80,000 km² is in western Jilin Province (Fig. 1) [25]. During the Late Cretaceous, the Songliao Basin was in the postrift thermal subsidence stage with two large-scale lake expansions [24]. Meanwhile, two deep-water lacustrine oil shale-bearing strata were deposited, namely the Qingshankou Formation (K_2qn) and the Nenjiang Formation (K_2n). There are 5 layers of dark gray or gray-black recoverable oil shale in the first member (K_2qn^1) of K_2qn, and 6 layers of dark gray recoverable oil shale in the first two members (K_2n^1 and K_2n^2) of K_2n in

Nong'an County, southeast of the basin. The oil yield of K_2qn^1 and K_2n^{1-2} oil shales may reach 9.31 and 12.10 wt%, respectively [1, 22, 23].

2.3. Luozigou Basin

The Luozigou Basin is siuated in Wangqing County, northeast of Jilin Province, and covers an area of about 200 km² (Fig. 1). It is a Mesozoic nonmarine extensional basin mainly filled with the Lower Cretaceous Dalazi Formation (K_1dl) [1, 22, 23]. The regional structure of this basin belongs to the northern terminal of the Liangjiang-Antu tectonic belt [26]. K_1dl can be further divided into two members: the lower member (K_1dl^1), which comprises conglomerate, sandstone and shale, and the upper member (K_1dl^2), which chiefly consists of oil shale interbedded with sandstone. K_1dl^2 has 7 layers of gray-to-black recoverable oil shale, with medium oil yield (average 6.72 wt%, maximum 14.37 wt%), predominantly deposited during the transgressive systems tract (TST) and the highstand systems tract (HST) [1, 26].

3. Samples and methods

3.1. Sampling

The age, unit name and other information on four oil shale samples studied in this article are given in Table 1. Sample FT collected from an underground mine of the Huadian Basin can be ignited with a lighter. This sample is so tight and rigid that it is difficult to cut with a hammer or an electric circular saw. Two of the samples, NJ and QSK, with obvious lamellation were procured from outcrops in Nong'an County, and sample NJ contains a large number of macroscopic fossils, e.g., conchostracans, ostracods. Sample LT gathered from an underground mine of the Luozigou Basin is combustible, tight and rigid as sample FT.

   Each sample contains several hand specimens obtained from different oil shale-bearing layers at the same sampling location, which not only reduces the effect of heterogeneity but also expands the representativeness of the study. Each oil shale specimen was subsampled two times. From each specimen (1) ~1 cm³ × 2 chips for broken surfaces SEM imaging, i.e., conventional SEM imaging; and (2) ~1 cm³ × 5 chips for ion-polished surfaces SEM imaging were prepared. Both broken and ion-polished surfaces contained cross sections perpendicular and parallel to bedding for 2D pore characterization in two important orientations.

3.2. Sample preparation

Sample preparation and SEM imaging in this study were performed at the Microstructure Laboratory for Energy Materials, China University of Petroleum (Beijing).

To avoid artifact pores (including fractures) produced by hammering, some broken surfaces were prepared according to the procedure used by O'Brien and Slatt [27]. All of the broken surfaces were then dedusted and dried.
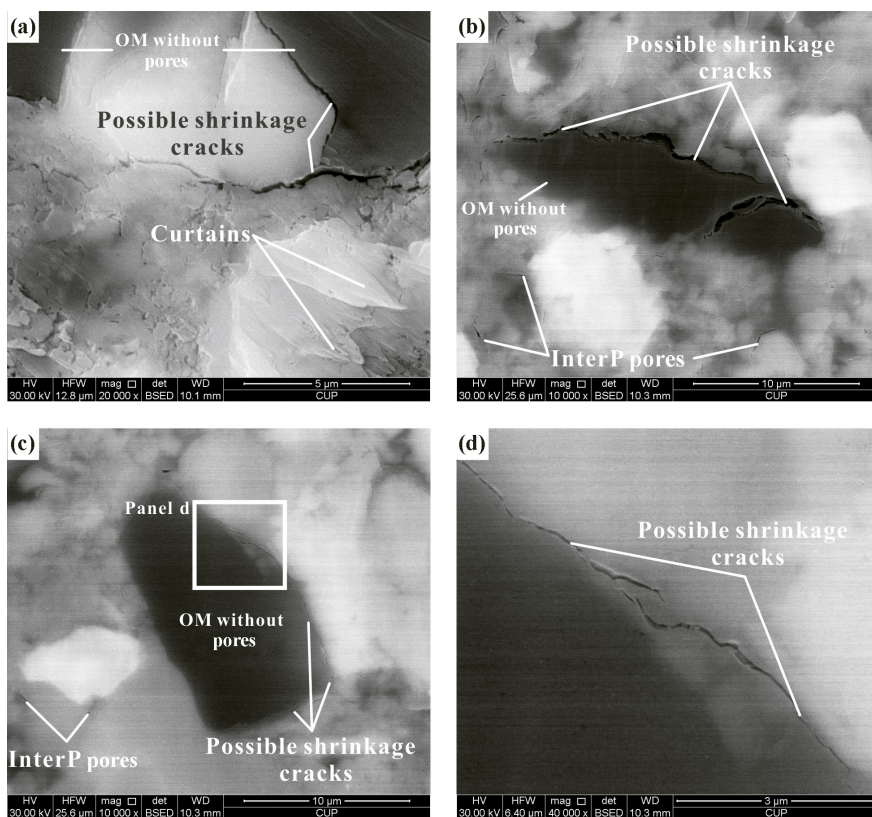

Fig. 2. Common artifacts within ion-polished surfaces of sample LT. Possible shrinkage cracks within or along with OM may be formed during desiccation, decompression or sample preparation. These organic matters show similar darker grayscale colors without pores: (a) noticeable wedge-shaped curtains produced by Ar ion polishing on the bottom right of the view; (b)–(c) interP pores (elongated grain-rim pores) on the bottom of the view; (d) enlargement of white-framed area in (c) showing possible shrinkage cracks at microscale. Abbreviations: HV – high voltage (accelerating voltage); HFW – horizontal frame width; mag – magnification; det – detector; BSED – backscattered electron detector; ETD – Everhart-Thomley detector; WD – working distance; CUP – China University of Petroleum.

We chose damage-free chips for Ar ion polishing. The chips were air dried, dry polished to create a smooth surface using abrasive paper, and polished by Leica EM RES102 under a 5° incident angle at 5 kV and 2.2 mA for 6 h [5]. The ion-polished surface of each chip is approximately 10 mm^2.

Lastly, both the broken and ion-polished surfaces of oil shale chips were coated with very thin conductive gold by using Leica EM SCD500 at 20 mA for 120 s to enhance conductivity during SEM imaging.

It is worth noting that other artifacts (e.g., shrinkage cracks, curtaining, redeposition, ion-beam striations) associated with sample preparation (e.g., drying, mechanical polishing, Ar ion polishing) may be mistaken for pores, but these artifacts can be easily identified based on close observation and practical experience (Fig. 2) [15, 21, 28].

3.3. SEM imaging

The samples were examined using FEI Quanta 200F, an FE-SEM. The detectors used in the study included an ETD, a second electron (SE) detector, for observing topographic variation, a BSED for compositional information, and an energy-dispersive X-ray spectroscopy (EDS) for identifying minerals [15].

Differently from SE images acquired from the broken surfaces of oil shale for morphological observation as previously noted, BSE images are often acquired from ion-polished surfaces for characterizing composition variation [7, 14]. The BSE image contrast (grayscale variation) indicates compositional (mean atomic number, Z) differences in the sample [20]. The grayscale value in the BSE image is positively correlated with Z. The higher the Z, the higher the image contrast, and vice versa. For example, in grayscale digital images, pyrite (high Z) will be bright white; quartz and feldspar (mid Z) will be mid-gray; OM and pore (low Z) will be dark gray to black [18, 19].

All analyses were performed at room temperature of ~23 °C and relative humidity of ~35%. The working distances of the system in this investigation were 8.4 to 13.4 mm. Apparatus magnification ranged from 25x to 200,000x. The FE-SEM images of ion-polished surfaces were taken at an accelerating voltage of 30 kV with a maximum resolution of ~1.2 nm.

4. Results

Pores within oil shale samples are described in this article using the mudrock pore classification scheme by Loucks et al. [15]. This scheme is simple, practicable, and consistent with the pore classification applied in sandstone and carbonate reservoir systems. The scheme defines three fundamental types of pores: 1) interparticle (interP) pores between particles (e.g., pores between minerals, between mineral and OM, between OM and fossil, pores defined

by a framework of mineral particles); 2) intraparticle (intraP) pores within particles except for OM (e.g., pores within the fossil, intercrystalline pores associated with pyrite framboid, pores caused by partial dissolution, pores within the cleavage of the particle); and 3) OM pores defined as intraP pores within OM.

4.1. Particles

Pores are void spaces between or within particles, so it is necessary to investigate the component and morphological features of particles before identifying pore types. Oil shale is a fine-grained argillaceous clastic rock and its constitutive particles are mainly composed of fossils, minerals and OM. It is difficult to distinguish the latter two only from the morphology observation, especially when determining mineral species. Using the BSE detector with an EDS detector can help solve the problem quite easily.

4.1.1. Fossils

The fossil particles are predominantly composed of ostracods, bivalves and cyanobacteria (Fig. 3). Most of these fossils range in size from 5 μm to 5 mm, and some even exceed 1 cm. Fossils predominantly do not show obvious changes in shape, size and grayscale under SEM, indicating that few of them undergo dissolution, but some fossils such as bivalves exhibit signs of recrystallization under a polarizing microscope. Fossils are overwhelmingly also rigid grains that resist compaction. In the SE images of broken surfaces, fossils not only maintain the original textures on shells but also preserve the appearance characteristics of a "stack of poker chips" in hormogonia (Fig. 3a–c). In the BSE images of ion-polished surfaces, fossil fragments are often similar in grayscale but vary in shape (e.g., tulwar, horseshoe), which is related to their original shape and cutting angle (Fig. 3d–f). Moreover, fossils are often the largest particles (in area) in most fields of the view (Fig. 3). Therefore, these remains are the most readily identified among the three particles.

4.1.2. Minerals

Quartz, pyrite, clays (e.g., illite, kaolinite, chlorite, mixed-layer clays) and feldspars (e.g., albite, orthoclase) are the common mineral components of oil shale, and the origin of these minerals is partly authigenic and partly detrital. It should be noted that minerals such as quartz and feldspars may have both origins, especially the authigenic overgrowth and replacement.

Authigenic minerals (e.g., pyrite, clays) usually exhibit an appreciable degree of crystal habit with straight margins (Figs. 4, 5b–c). For example, in Figure 4, in the SE images of broken surfaces, pyrite mostly appears as a spherical framboid (clusters of crystals), and a single euhedral pyrite crystal
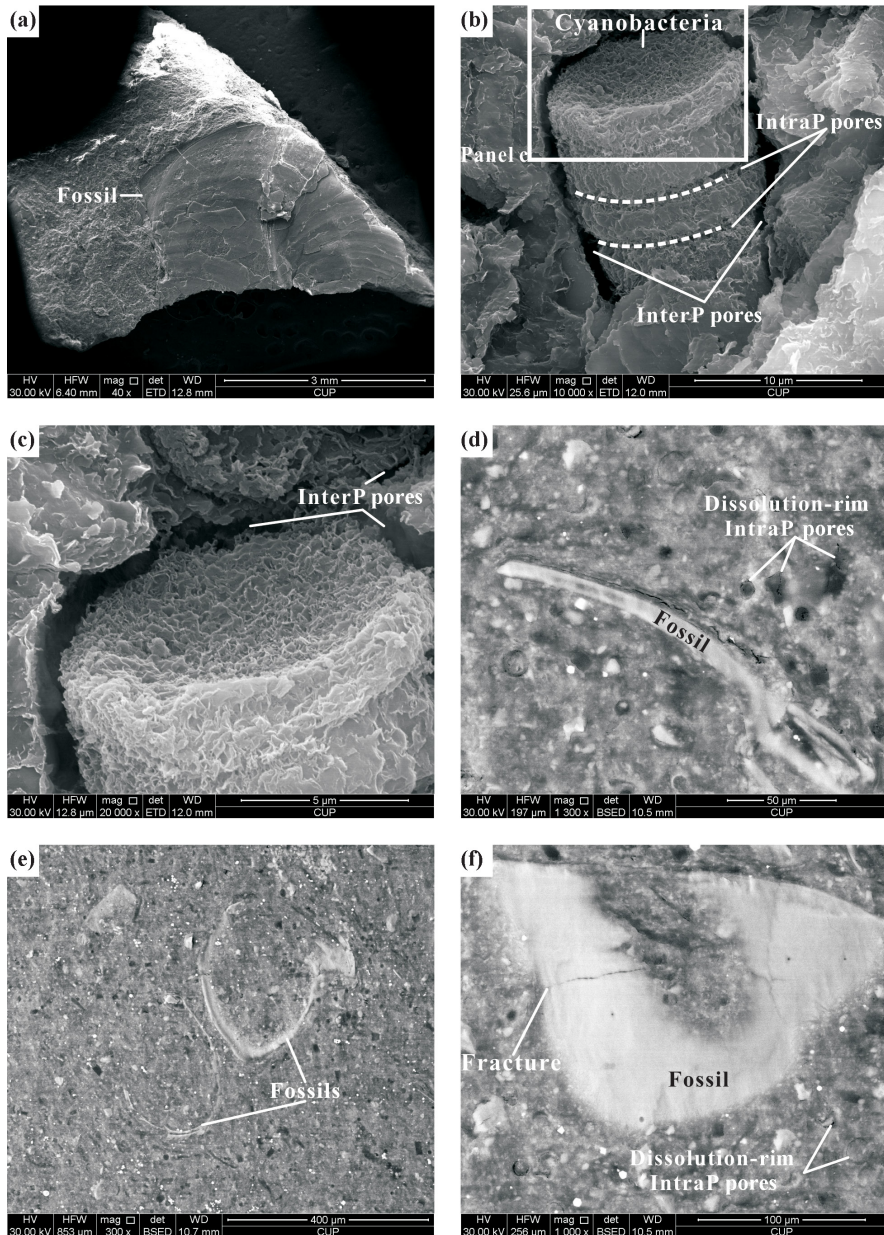
Fig. 3. Examples of fossil particles and pores within oil shales: a) cross section oriented parallel to bedding plane showing a fossil fragment with conchoidal features and lamellar laminae (low-magnification SE image of sample NJ); (b) hormogonia of cyanobacteria surrounded by cylindrical interP pores in the center of the view; intrafossil pores (dash) circling the hormogonia parallel to each other; notice the clay flakes wrapping around the bottom edge of the hormogonia (SE image of the broken surface of sample FT); (c) enlargement of white-framed area in (b) showing details of concave and body-cavity pores within the hormogonia; see the interP pores between hormogonia and other particles also present; (d) fossil fragments in the center and bottom right of the view showing a tulwar shape; notice the many dissolution-rim pores having a variety of shapes from irregular to rounded; (e)–(f) similar to (d); (f) nearly a full of the view showing a piece of fossil fragment with intrafossil fracture. Images (d)–(f) are BSE images of the ion-polished surfaces of sample FT.
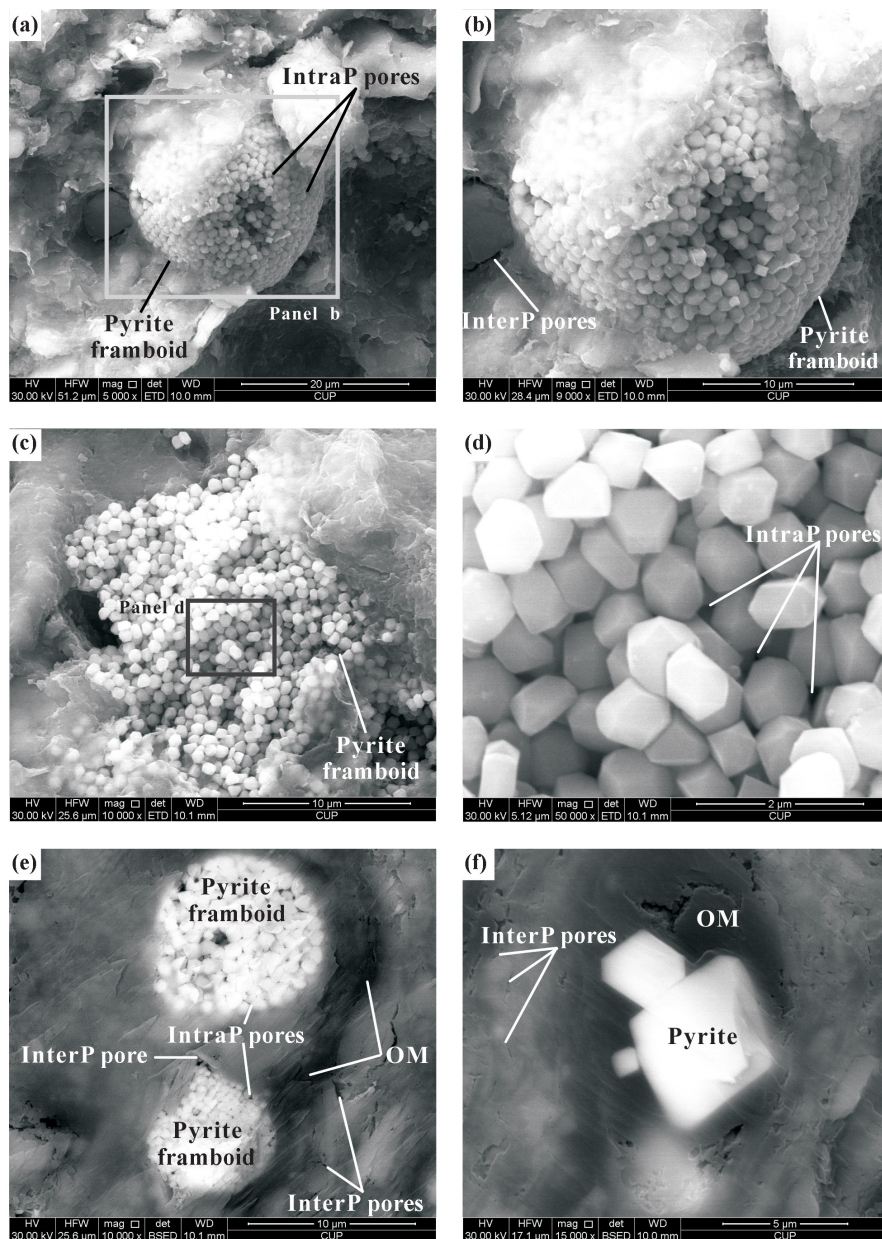
Fig. 4. SEM images of pyrite and pores within oil shales, with most pyrite crystals being euhedral: (a) strawberry-like pyrite framboid in the center of the view; notice the clays draped over the pyrite framboid like strawberry sepals (SE image of the broken surface of sample NJ); (b) close-up view of gray-framed area in (a) showing details of plentiful intraP pores between pyrite crystals within pyrite framboid; see the grain-rim pores around mineral particles on the left of view; (c) clays wrapping around the edge of loosely packed pyrite framboid (SE image of the broken surface of sample NJ); (d) close-up view of black-framed area in (c) showing no cement filling intraP pores within pyrite framboid; (e) two pyrite framboids (bright white) in the center of the view with lots of pores partly filled with OM between pyrite crystals; notice the grain-rim pores along mineral particles boundaries (bottom right) and triangular framework pores (center) between clays also shown in this BSE image of the ion-polished surface of sample NJ; (f) OM with a smooth surface (dark gray) around three euhedral pyrite crystals (bright white); see the grain-rim pores along with angular mineral particles (left) also present (BSE image of the ion-polished surface of sample FT).

usually presents a pyritohedron shape. In the BSE images of ion-polished surfaces, pyrite framboids appear with a rounded shape and bright white color, and the single euhedral pyrite crystal mostly presents a nearly hexagonal shape. Authigenic minerals range in size from less than a micrometer to 30 μm.

Detrital minerals such as quartz and feldspars often appear as discrete crystals, not clusters. For example, in Figures 5 and 6, in the SE images of broken surfaces, the orthoclase crystal appears with well-developed cleavages surrounded by clays. In the BSE images of ion-polished surfaces, detrital minerals occur with similar gray-white to mid-gray color adjoined with other particles. These minerals are seldom euhedral and often occur with irregular shape. The substantial edges of detrital minerals are often rounded but a few remain straight in BSE images. The grain size of detrital minerals ranges from 2 μm to 100 μm and is generally larger than that of authigenic minerals.

In BSE images, minerals and OM can be quickly distinguished mainly by backscatter signal contrast (Figs. 2, 4e–f, 5f, 6d–f). However, in the SEM observation of both broken and ion-polished surfaces, it is difficult to accurately identify minerals except for euhedral and framboidal pyrites by examining morphology (e.g., grain boundary, crystal habit, cleavage plane) and grayscale. So it is necessary to use EDS data to distinguish different minerals (Figs. 5–6). A typical x-ray spectrum obtained by the EDS detector is shown on the bottom left of Figure 6f. The characteristic x-ray peaks of Si, Al, K and O imply the presence of orthoclase.

4.1.3. Organic matter

Oil shale is a solid combustible sedimentary rock with high OM content [23]. The oil yield values of the four samples are all above 3.50 wt%, which indicates that OM is an ordinary particle in SEM images. OM occupies a space between the other two particles and has a variety of shapes from irregular to triangular to ellipsoidal to elongated by compaction (Figs. 2, 4e–f, 6d–f, 7a–b). Its particle size ranges from micrometer to sub-millimeter. No matter its appearance in the broken or ion-polished surface images, OM always occurs as a homogeneous and smooth material with a similar darker grayscale value (Figs. 2, 4e–f, 5f, 6d–f, 7a–b).

4.2. Pore types

Pores commonly exhibit darker to black grayscale value in both SE and BSE images, being even lower than that of OM in the same field of the view, so they are relatively easy to identify in photomicrographs.

4.2.1. InterP pores

InterP pores are voids between particles such as clay platelets, quartz, feldspars, fossils and OM. The size of most interP pores ranges from 100 nm to 2 μm,

but values exceeding 5 μm are also common. InterP pores generally appear between mineral and mineral particles or between mineral and OM particles. Many pores are elongated along the boundaries surrounding particles (Figs. 2b–c, 4b, 4f, 5e–f, 6d–e, 7a). At the same time, other pores (i.e., framework pores) are sharply irregular to polyhedral to triangular inside frameworks formed by the stacking of particles (Fig. 4e). Some are cemented by OM or minerals (e.g., pyrite, clays), resulting in multiple grayscale values in BSE images of ion-polished surfaces (Fig. 6f). InterP pores also occur between fossils and other particles. Figures 3b–c reveal that in sample FT barrel-like pores surround the cyanobacteria.

It must be pointed out that ion polishing may produce a significant heating effect on the non-conductive particles (e.g., OM) together with other sample preparation processes (e.g., drying, mechanical polishing), causing these particles to shrink and form artificial interP pores (artifacts), especially pores along the rims of minerals related to OM may represent shrinkage cracks (Fig. 2) [29, 30].

4.2.2. IntraP pores

IntraP pores are voids inside particles such as pyrite, clays, feldspars, and fossils, except OM. We found four common subtypes of intraP pores within oil shale samples: 1) intrafossil pores, 2) pyrite intercrystalline pores, 3) dissolution pores, and 4) cleavage pores (e.g., within clays) [15]. The size of intraP pores varies with subtype, but is generally at the micro- to nano-scales.

The intercellular pores within cyanobacteria shown in Figure 3b–c are generally annular and perpendicular to the long axis direction of hormogonia. In addition, there are concave pores at the top and bottom of every hormogonium and body-cavity pores within cyanobacteria.

Because oil shale contains a large number of pyrite framboids, inter-crystalline pores between crystals within pyrite framboids are the most common subtype of intraP pores (Fig. 4a–d). Many of these pores are filled with clays and OM (Fig. 4e).

Chemically unstable particles such as feldspars (e.g., anorthite) and a small number of fossils can occur in numerous pores during the dissolution process (Fig. 3d–f). Dissolution pores often appear at the rims of particles, resulting in the grayscale value of the dissolved area becoming darker in the BSE images of ion-polished surfaces (Fig. 6a–b). Due to the observation angle and strong topographic variations within the broken surfaces, dissolution pores were rarely found in the SE images. For accurate pore characterization, it is necessary to carefully identify the artificial dissolution pores generated by the differential Ar ion polishing.

Cleavage pores are voids mainly inside the cleavage planes of clay particles (e.g., chlorite, illite, smectite, mixed-layer clays) (Fig. 5c). These pores are frequently parallel to one another, some are distorted by compaction, and some are cemented by authigenic minerals (Figs. 5e, 6c).
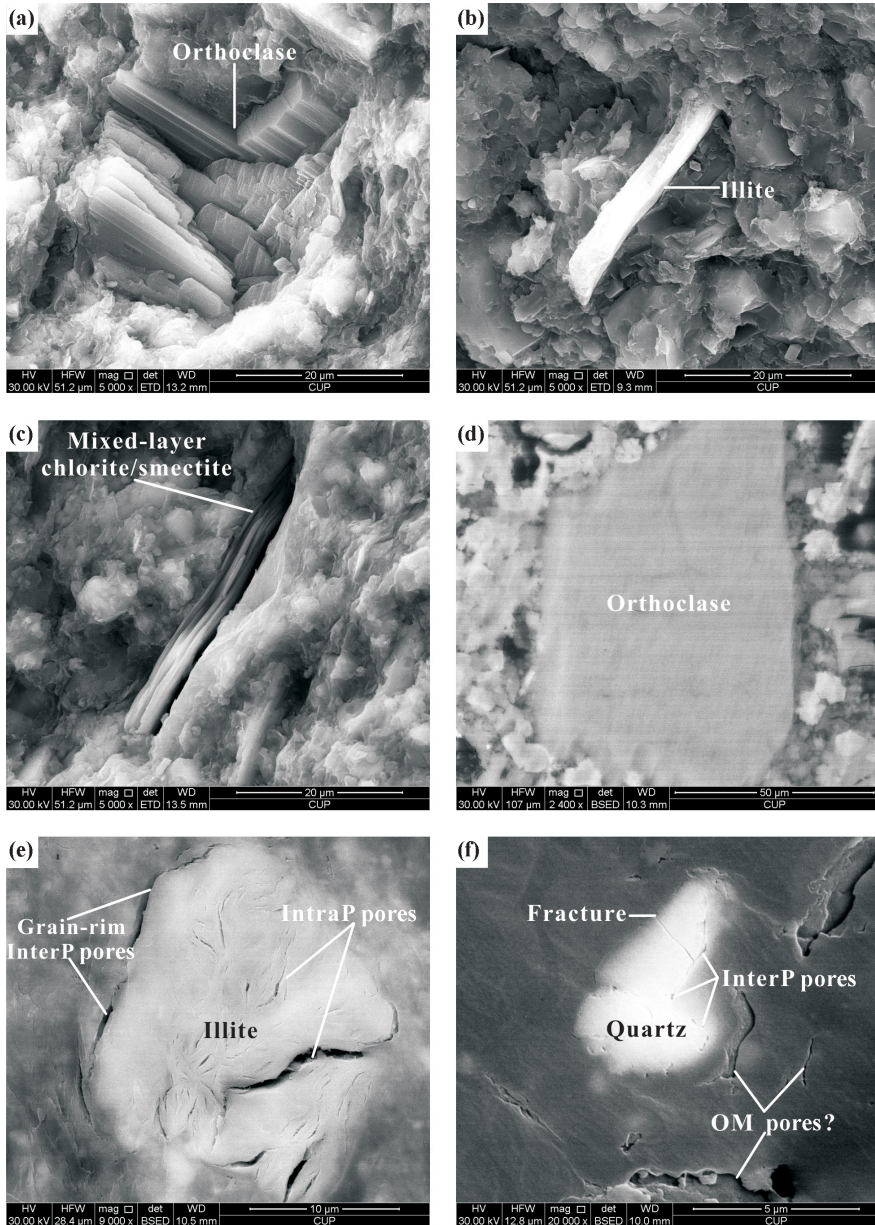
Fig. 5. Examples of mineral particles and related pores within oil shales identified by EDS analysis: (a) orthoclase with well-developed cleavages; (b) mineral particle with bright color illite in the center of the view; (c) mixed-layer chlorite/smectite with well-developed cleavages; (images (a)–(c) are SE images of the broken surfaces of sample LT); (d) orthoclase with gray color in the center of the view present in the BSE image of the ion-polished surface of sample LT; (e) inside and around illite the deformed intraP pores located between clay flakes and elongated grain-rim pores, respectively (BSE image of the ion-polished surface of sample FT); (f) elongated grain-rim pores around the angular quartz and a facture stretch across the body of the mineral; note the possible formation of OM pores during sample preparation (BSE image of the ion-polished surface of sample NJ).
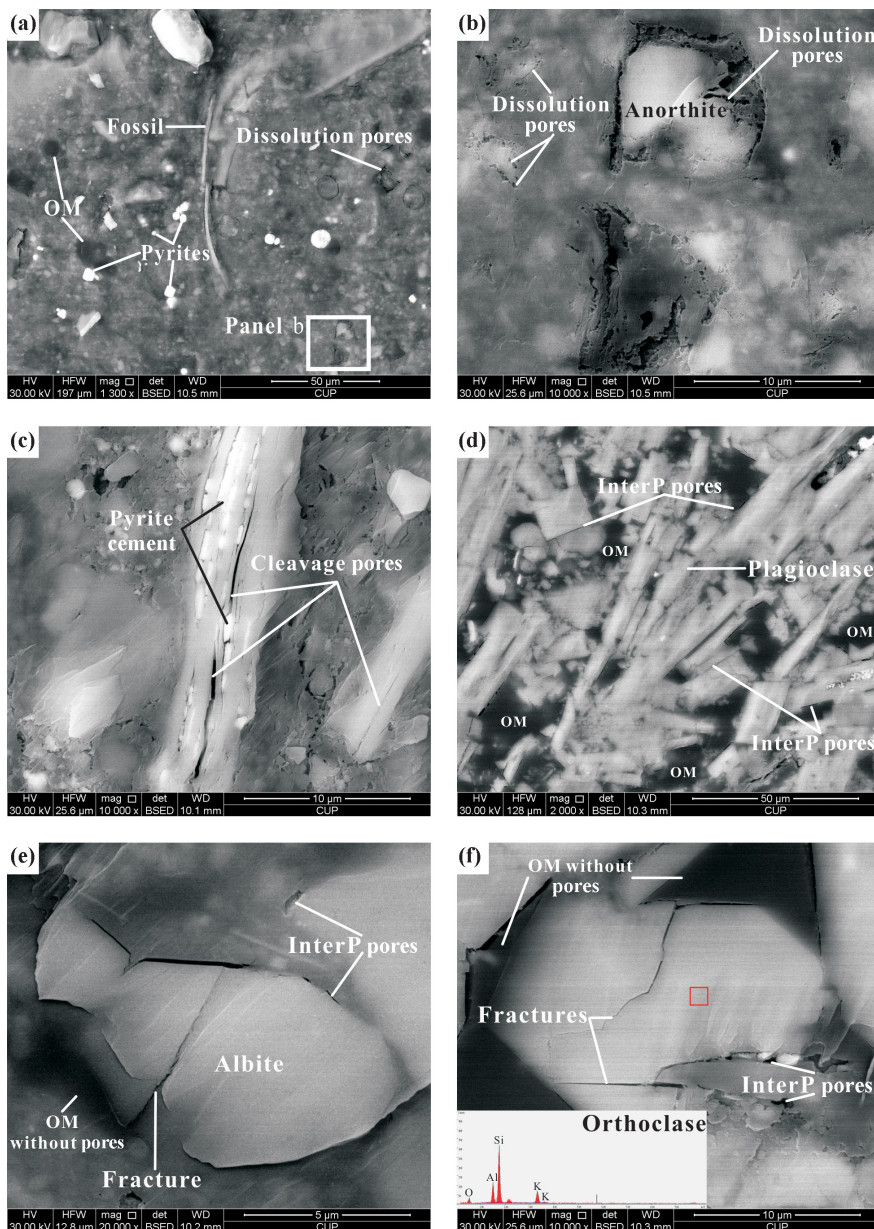
Fig. 6. Examples of pores within oil shales: (a) irregular to rounded shape dissolution pores scattered throughout the cross section, mainly on the right of the view; pyrite crystals and framboids (bright white) disseminated throughout the matrix of oil shale present (BSE image of the ion-polished surface of sample FT); (b) close-up view of white-framed area in (a) showing details of dissolution voids in or around the body of anorthite without cement; (c) pyrite crystals present between clay sheets like peasecod; note some cleavage pores being voids without pyrite cement (BSE image of the ion-polished surface of sample NJ); (d) straight grain-rim pores scattered throughout the cross section; (e) fracture extended across the body of albite and other particles; notice the grain-rim pores and OM without pores present; (f) fractures cut through the orthoclase and intersect (chemical analysis (EDS line graph) of the mineral particle in the red-framed area); see the interP pores cemented by minerals and OM without OM pores present. Images (d)–(f) are BSE images of the ion-polished surfaces of sample LT.

4.2.3. Organic matter pores

Pores in OM are voids present in it. These pores are rare within oil shale samples, and mostly OM is tight and pore-free (Figs. 2, 4e–f, 5f, 6d–f, 7a–b). As pointed out by Loucks et al. [15], in mudstones with the vitrinite reflectance (R_o) value less than 0.6%, OM pores rarely appear. Due to the low thermal maturity of four oil shale-bearing formations, we only found a small number of OM pores in sample QSK with the highest level of maturity (~0.76% R_o) (Fig. 7c–f) [23]. The size of these pores observed in BSE images ranges from 10 nm to a micrometer and should increase during Ar ion polishing. The shape of OM pores varies widely, from irregular to rounded to bubble-like to elliptical. Some OM pores tend to appear in clusters and generally are of sponge shape. We often observe isolated and irregular voids within OM in the BSE images of ion-polished surfaces, especially at the edge of OM, which may be artifacts associated with sample preparation (Figs. 4e–f, 5f).

4.2.4. Fracture pores

Fracture pores are rarely included in the well-known pore classification schemes of mudrocks in earlier researches [15–17]. Even the scheme of Loucks et al. [15] contains no information on fracture pores. Fractures are occasionally observed in images, and these pores can be very vital in oil shale evaluation and in-situ conversion. Although some fractures may be formed during desiccation, decompression, or sample preparation, we picked out several SEM images of submicron fractures considered to be originated from sedimentation. Some fractures occur within a single rigid particle (e.g., fossil, feldspar, quartz), and some fractures can penetrate particles of different hardness and form an effective pore network with interP pores (Figs. 3f, 6e–f).

4.3. Cross section orientation

The laminations within the oil shale do not show linear features due to compaction, but curved surfaces with unevenness (Fig. 8). Therefore, the cross section parallel to bedding is difficult to characterize. However, the broken surface SEM imaging of a section that is parallel to the bedding (e.g., Fig. 3a) can sometimes reveal textural characteristics of particles such as microfossils.

In recent studies, the most commonly used cross section orientation in the ion-polished surface SEM imaging of shale is perpendicular to bedding [15, 17, 19, 21, 31, 32]. Besides facilitating the observation of pore characteristics, this section also provides the distribution and content of OM in shale, as well as other sedimentary information for further study (Fig. 8).

In addition, through high-resolution SEM observation, we found that particle stratification is common in the cross section perpendicular to bedding, especially the banded distribution of OM (Fig. 8). This finding, while preliminary, may help us understand the significant anisotropy of mechanical
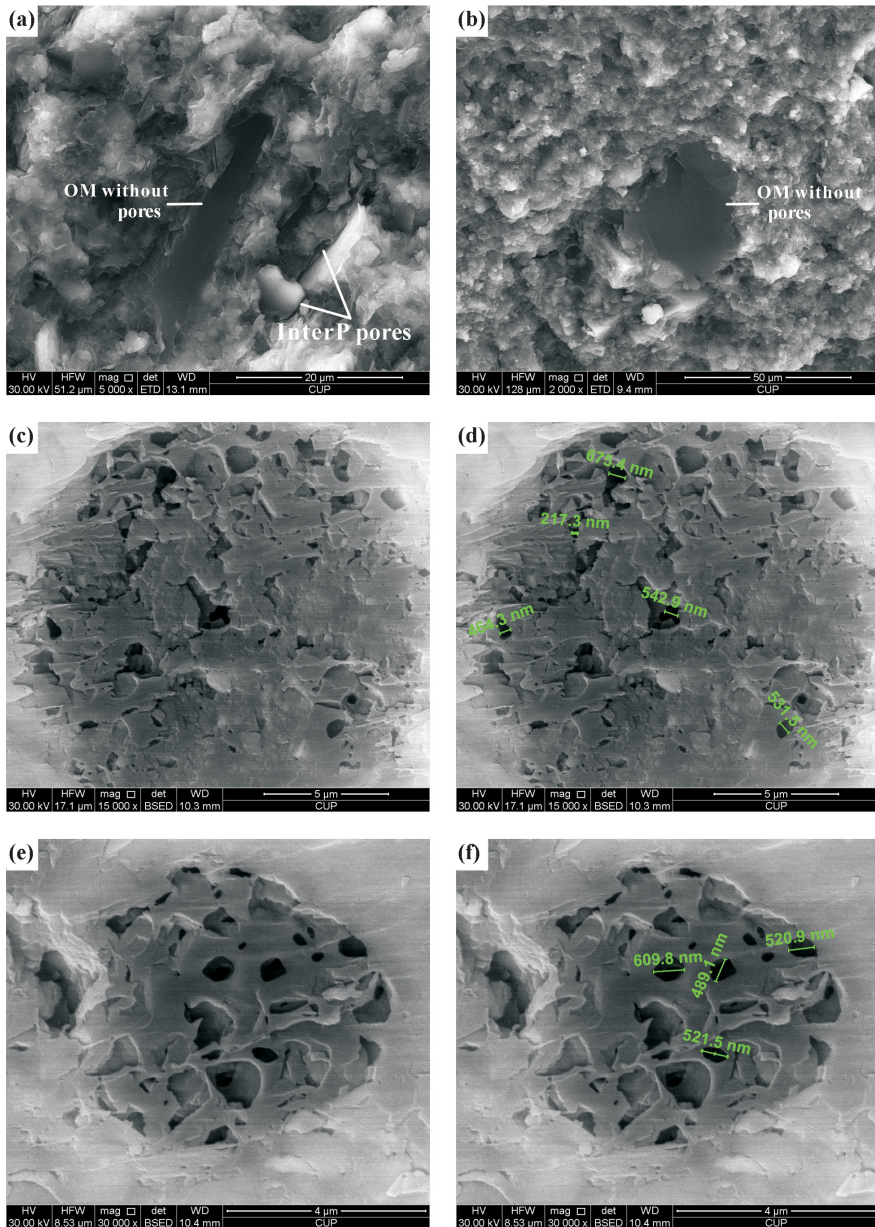
Fig. 7. Examples of OM and pores within oil shales: (a) banded OM having a smooth surface texture and similar darker grayscale color without pores in the center and on the bottom of the view; see the elongated grain-rim pores between different mineral particles on the bottom right of the view; (b) similar to (a); (images (a)–(b) are SE images of the broken surfaces of sample LT); (c)–(f) OM with mainly irregular- to elliptical-shaped nanoscale pores. Images (c)–(f) are BSE images of the ion-polished surfaces of sample QSK.
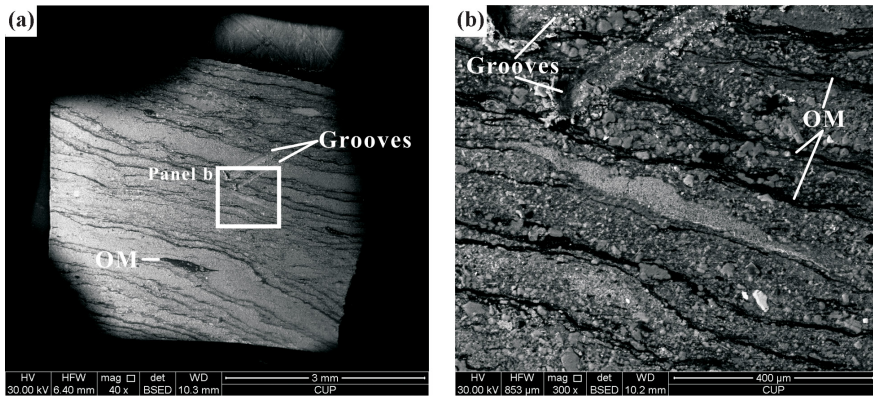
Fig. 8. BSE images of ion-polished cross section oriented perpendicular to bedding of sample LT: (a) low-magnification view showing the laminated microtexture of oil shale to consist of OM (black) interbedded with numerous mineral particles (gray), these laminations being roughly parallel to bedding plane; (note the two grooves during sample preparation on the upper right of the view and a piece of lenticular OM on the center bottom of the view); (b) enlargement of white-framed area in (a) showing details of distorted OM and mineral laminations partly due to differential compaction.

properties (e.g., elastic modulus (E)) and thermal properties (e.g., thermal conductivity (TC)) within oil shale [33–35].

5. Discussion

5.1. Comparison between broken and ion-polished surface SEM imaging

With the advantages of quickness, convenience and cost-saving, the broken surface SEM imaging has been used in previous studies on oil shale reservoir characterization for a long time [23, 36, 37]. Although in recent years the use of this technique in unconventional oil and gas studies has gradually decreased, it can provide more abundant topographic information about primary fabric without disruption by polishing (i.e., mechanic polishing and Ar ion polishing) (Figs. 3a–c, 4a–d, 5a–c) [4].

Considering the relatively high costs of some other techniques, ion-polished imaging has gained popularity in unconventional oil and gas studies. The obtained ultrasmooth surfaces applicable for high-resolution SEM imaging are beneficial to the observation of pores, minerals, and OM, and also enable a further quantitative characterization of porosity and OM content by using different image analysis software such as ImageJ and JMicroVision [18].

However, it is worth mentioning that due to heating, vacuum, and differential polishing during the Ar ion polishing process, a large number of artifacts (e.g., shrinkage cracks, artificial dissolution pores) can be produced,

the size of some pores enlarged and even the reflectance of OM on the polished surface changed, which, however, needs to be carefully recognized and distinguished [38, 39]. To reduce artifacts during Ar ion polishing, future investigations using liquid nitrogen cooling, shallow beam angles, and lower acceleration voltages are therefore suggested [39, 40].

5.2. Pore types distribution

All four oil shale samples from formations in Jilin Province contain interP and intraP pores, except for OM pores, which are only moderately distributed in sample QSK. There are also small differences in the amount of OM pores between the samples. In Table 2 the distribution of different pore types in oil shale samples is presented. Sample LT has more debris particles (feldspars, quartz), resulting in the most developed intercrystalline (interP) pores among the four samples (Fig. 6d–f). Sample NJ has the highest pyrite content, and pyrite intercrystalline (intraP) pores are widely spread, while sample QSK has the lowest pyrite content and pores of this type are rare (Fig. 4a–e). A large number of millimeter-scale fossils scatter along the bedding planes of sample NJ, and the high content of microfossils (cyanobacteria) in sample FT leads to the frequent occurrence in intrafossil (intraP) pores in it (Fig. 3). Due to the partial dissolution of chemically unstable particles (feldspars, fossils), dissolution (intraP) pores are common in sample FT, while these pores are rare in the remaining three samples (Figs. 3d–f, 6a–b). Sample FT has the highest OM content (showing lenses and bands) but no OM pores, while sample QSK has a medium content of OM with minor pores (Fig. 8c–f). These findings will help us choose a more efficient in-situ conversion method for oil shales in Jilin Province with less underground environmental pollution [5, 6].

Table 2. Distribution of pore types in oil shale samples

Sample ID	InterP pores	IntraP pores	OM pores
FT	Minor	Dominant with largest intrafossil and dissolution pores	Undiscovered
NJ	Common with intercrystalline pores and minor framework pores	Dominant with largest pyrite intercrystalline pores	Undiscovered
QSK	Dominant	Minor with rare pyrite intercrystalline pores	Minor
LT	Dominant with largest intercrystalline pores	Minor	Undiscovered

5.3. Comparison with North American gas shales SEM imaging

The microstructure of gas shales in North America, e.g., Barnett shale, Eagle Ford shale, Woodford shale, Haynesville shale, Marcellus shale, has been thoroughly studied and some well-known pore classification schemes of mudrocks have been derived from the respective investigations [15–17, 30]. Although both being mudrocks, comparison has revealed three main differences in microstructure between gas shale and oil shales:

1. Carbonate content. According to Liu et al. (Table 2, [1]), the four oil shale-bearing formations in Jilin Province contain almost no carbonate except for the Huadian Formation, which contains abundant carbonate (~25%). However, as pointed out by Erdman and Drenzek (Table 2, [41]), all the four North American shale gas producing formations, i.e., Marcellus, Haynesville, Woodford, and Barnett, contain carbonates up to 38%. The higher carbonate content implies the presence of more compaction-resistant minerals, which can form framework (interP) pores, as well as the presence of more chemically unstable minerals (e.g., calcite, dolomite), which can form dissolution (intraP) pores [21].

2. Fossils. North American gas shales have more types and a higher amount of fossils than oil shales in Jilin Province observed under SEM, which can result in a higher quantity of intrafossil (intraP) pores [15, 19, 31, 32]. In addition, the increase in the number of chemically unstable calcareous fossils (e.g., foraminifera, coccoliths) may also increase the amount of dissolution (intraP) pores [19].

3. OM and OM pores. Comparison of the SEM images reveals that oil shales in Jilin Province have a higher content of OM, which appears as patches, lenticles or continuous bands up to a few millimeters in size, differently from gas shales in North America, whose OM content corresponds to their total organic carbon (TOC) content, while at the same time, their OM has fewer pores (Fig. 8) [1, 41]. In addition, more ductile OM may fill some interP and intraP pores, which possibly reduces the total porosity of oil shales [42].

These differences between Chinese oil shales and North American gas shales may be due to their diverse sedimentary environments and levels of maturity [1, 5, 15, 18–20, 31, 32, 41]. The continental sedimentary environment provides an abundant supply of siliciclastic sediments such as quartz and feldspars for oil shales in Jilin Province [1, 22–24, 26]. The marine sedimentary environment not only allows North American gas shales to have significant carbonate contents but also provides enhanced nutrient supply for marine organisms [19]. The shallowly buried oil shales in Jilin Province deposited since the Early Cretaceous have low maturity (R_o(max.) $\leq 0.76\%$) [1, 23]. The gas shales in North America, represented by the reservoir systems of Barnett, Woodford and Marcellus, were formed at earlier ages and deep burial with higher maturities [41].

5.4. Effect of oil shale diagenesis

High-resolution SEM imaging can not only characterize the nanoscale pore structure within oil shale but also provide much solid evidence left by the diagenetic processes of this sedimentary rock.

The deformed bedding planes and fractured rigid particles (e.g., fossils, feldspars) in photomicrographs are imprints of mechanical compaction on oil shales in Jilin Province (Figs. 5f, 6a, 6e–f, 8). In addition, compaction largely decreases the original volume and porosity (interP and intraP pores) of these oil shales. During this time, the ductile OM and other particles may enter these pores and also reduce porosity [15]. But there is still a small amount of interP pores (e.g., framework pores) that are preserved in pressure shadows and compaction protected spaces adjacent to rigid particles (Fig. 4e) [17, 21].

Sedimentary pyrite, including single euhedral crystals, clustered euhedral crystals and framboids widely distributed in oil shale, may be formed due to the supply of decomposable OM during shallow burial (Figs. 4, 6c) [15, 43, 44]. Also, the smectite-to-illite conversion occurred during the shallow to intermediate burial of oil shale (Fig. 5c) [15, 17, 21]. Furthermore, some particles, especially feldspars in the studied oil shales, dissolved possibly due to the carboxylic and phenolic acids produced by the decarboxylation of OM (Figs. 3d, 3f, 6a–b) [15, 17, 21, 44]. The dissolution seldom removes all particles, and only partially corrodes the margins of the particles. With increasing burial depth, oil shale becomes thermally more mature and can develop OM pores (Fig. 7c–f). Therefore, it is possible to preliminarily judge whether oil shale has reached thermal maturity by observing the existence of OM pores.

6. Conclusions

Pores within oil shale samples from four formations in Jilin Province, Northeastern China have been imaged, decribed and classified using argon ion polishing and field emission-electron scanning microsopy techniques. The results of this study lead to the following conclusions:
1. Argon ion polishing can effectively reduce the relief on the observed surface for SEM imaging, but it is necessary to identify the accompanying artifacts (e.g., curtaining, redeposition, shrinkage cracks) and enlargement of pore sizes. While ion-polished surfaces and cross sections perpendicular to bedding are commonly used in shale systems studies, observation together with broken surfaces and cross sections parallel to bedding can more comprehensively characterize the microstructure of oil shale.
2. The particles within the studied oil shales are composed of fossils, minerals and organic matter. Pores within oil shale are void spaces between or inside particles and three fundamental types are defined: interparticle,

intraparticle and OM pores. InterP pores are the most common, these are generally larger than the latter two with various shapes; intraP pores are prevalent and their shape changes with subtype; OM pores are rare with pore sizes mainly at the nanoscale.

3. Pores of the four oil shale samples studied consist of interP pores and intraP pores, but only sample QSK contains trace amounts of OM pores. Sample FT has a large number of intrafossil and dissolution (intraP) pores due to the abundance of microfossils and the dissolution most likely related to OM decarboxylation. Sample NJ contains a lot of pyrite minerals and has the largest number of pyrite intercrystalline (intraP) pores in contrast to sample QSK, whose amount of such pores is the lowest. Sample LT enriched with clastic particles such as quartz and feldspars contains a great amount of intercrystalline (interP) pores.

4. A comparative study revealed that the contents of particles and OM pores within oil shales in Jilin Province of Northeastern China and gas shales in North America are very different, which may be due to their dissimilar sedimentary environments and levels of maturity. In the continental sedimentary environment, the four studied oil shale-bearing formations in Jilin Province are rich in terrigenous detrital supply, and it is difficult to form abundant OM pores because of their low maturity probably due to shallow burial. In contrast, the North American gas shales, e.g., Haynesville, Woodford, Barnett, deposited in the marine sedimentary environment contain a large number of carbonates and fossils, and some of the shales are buried deeply with high maturity, which can form plentiful OM pores.

Acknowledgments

REFERENCES

1. Liu, Z., Meng, Q., Dong, Q., Zhu, J., Guo, W., Ye, S., Liu, R., Jia, J. Characteristics and resource potential of oil shale in China. *Oil Shale*, 2017, **34**(1), 15–41. http://doi.org/10.3176/oil.2017.1.02

2. Deng, S. *Sub-Critical Water Extraction of Organic Matter from Oil Shale Lumps*. PhD thesis. Jilin University, China, 2013 (in Chinese).

3. Spain, D. R., McLin, R. SEM characterization of shale gas reservoirs using combined secondary and backscatter electron methods: An example from the Haynesville Shale, Texas and Louisiana. In: *Electron Microscopy of Shale Hydrocarbon Reservoirs* (Camp, W. K., Diaz, E., Wawak, B., eds.). American Association of Petroleum Geologists, Tulsa, OK, U.S.A., 2013, AAPG Memoir **102**, 45–52. http://doi.org/10.1306/13391704M102434

4. O'Brien, N. R., McRobbie, C. A., Slatt, R. M., Baruch-Jurado, E. T., 2016. Unconventional gas-oil shale microfabric features relating to porosity, storage, and migration of hydrocarbons. In: *Imaging Unconventional Reservoir Pore Systems* (Olson, T., ed.). American Association of Petroleum Geologists, Tulsa, OK, U.S.A., 2016, AAPG Memoir **112**, 43–64. http://doi.org/10.1306/13592016M1123692

5. Curtis, M. E., Sondergeld, C. H., Ambrose, R. J., Rai, C. S. Microstructural investigation of gas shales in two and three dimensions using nanometer-scale resolution imaging. *AAPG Bull.*, 2012, **96**(4), 665–677. http://doi.org/10.1306/08151110188

6. Desbois, G., Urai, J. L., Houben, M. E., Sholokhova, Y. Typology, morphology and connectivity of pore space in claystones from reference site for research using BIB, FIB and cryo-SEM methods. *EPJ Web Conf.*, 2010, **6**, 22005. http://doi.org/10.1051/epjconf/20100622005

7. Wang, Q., Liu, T., Liu, H., Qin, H., Li, S. Electron microscopy analysis of semi-coke from the microwave pyrolysis of oil shale with its fractal description. *Oil Shale*, 2010, **27**(3), 209–228. http://doi.org/10.3176/oil.2010.3.03

8. Kang, Z., Yang, D., Zhao, Y., Hu, Y. Thermal cracking and corresponding permeability of Fushun oil shale. *Oil Shale*, 2011, **28**(2), 273–283. http://doi.org/10.3176/oil.2011.2.02

9. Zhao, J., Yang, D., Kang, Z., Feng, Z. A micro-CT study of changes in the internal structure of Daqing and Yan'an oil shales at high temperatures. *Oil Shale*, 2012, **29**(4), 357–367. http://doi.org/10.3176/oil.2012.4.06

10. Tiwari, P., Deo, M., Lin, C. L., Miller, J. D. Characterization of oil shale pore structure before and after pyrolysis by using X-ray micro CT. *Fuel*, 2013, **107**, 547–554. http://doi.org/10.1016/j.fuel.2013.01.006

11. Saif, T., Lin, Q., Singh, K., Bijeljic, B., Blunt, M. J. Dynamic imaging of oil shale pyrolysis using synchrotron X-ray microtomography. *Geophys. Res. Lett.*, 2016, **43**(13), 6799–6807. https://doi.org/10.1002/2016GL069279

12. Kang, Z., Zhao, J., Yang, D., Zhao, Y., Hu, Y. Study of the evolution of micron-scale pore structure in oil shale at different temperatures. *Oil Shale*, 2017, **34**(1), 42–54. http://doi.org/10.3176/oil.2017.1.03

13. Konsa, M., Puura, V., Soesoo, A., Voolma, M., Aosaar, H. Petrography and mineralogy of the Attarat Um Ghudran oil shale, Central Jordan. *Oil Shale*, 2017, **34**(2), 110–128. http://doi.org/10.3176/oil.2017.2.02

14. Liu, H., Feng, S., Zhang, S., Xuan, H., Jia, C., Wang, Q. Analysis of the pore structure of Longkou oil shale semicoke during fluidized bed combustion. *Oil Shale*, 2020, **37**(2), 89–103. http://doi.org/10.3176/oil.2020.2.01

15. Loucks, R. G., Reed, R. M., Ruppel, S. C., Hammes, U. Spectrum of pore types and networks in mudrocks and a descriptive classification for matrix-related mudrock pores. *AAPG Bull*., 2012, **96**(6), 1071–1098. http://doi.org/10.1306/08171111061

16. Milner, M., McLin, R., Petriello, J. Imaging texture and porosity in mudstones and shales: Comparison of secondary and ion-milled backscatter SEM methods. In: *Canadian Unconventional Resources and International Petroleum Conference*, October 19–21, 2010, Calgary, Alberta, Canada. SPE Paper 138975-MS, 2010, 1–10. http://doi.org/10.2118/138975-MS

17. Schieber, J. Common themes in the formation and preservation of intrinsic porosity in shales and mudstones – Illustrated with examples across the Phanerozoic. In: *Society of Petroleum Engineers Unconventional Gas Conference*, February 23–25, 2010, Pittsburgh, Pennsylvania, U.S.A. SPE Paper 132370-MS, 2010, 1–10. https://doi.org/10.2118/132370-MS

18. Camp, W. K., Wawak, B. Enhancing SEM grayscale images through pseudocolor conversion: Examples from Eagle Ford, Haynesville, and Marcellus shales. In: *Electron Microscopy of Shale Hydrocarbon Reservoirs* (Camp, W. K., Diaz, E., Wawak, B., eds.). American Association of Petroleum Geologists, Tulsa, OK, U.S.A., 2013, AAPG Memoir **102**, 15–26. http://doi.org/10.1306/13391701M1021681

19. Jennings, D. S., Antia, J. Petrographic characterization of the Eagle Ford shale, South Texas: Mineralogy, common constituents, and distribution of nanometer-scale pore types. In: *Electron Microscopy of Shale Hydrocarbon Reservoirs* (Camp, W. K., Diaz, E., Wawak, B., eds.). American Association of Petroleum Geologists, Tulsa, OK, U.S.A., 2013, AAPG Memoir **102**, 101–113. http://doi.org/10.1306/13391708M1023586

20. Rine, J. M., Smart, E., Dorsey, W., Hooghan, K., Dixon, M. Comparison of porosity distribution within selected North American shale units by SEM examination of argon-ion-milled samples. In: *Electron Microscopy of Shale Hydrocarbon Reservoirs* (Camp, W. K., Diaz, E., Wawak, B., eds.). American Association of Petroleum Geologists, Tulsa, OK, U.S.A., 2013, AAPG Memoir **102**, 137–152. http://doi.org/10.1306/13391710M1023588

21. Schieber, J. SEM observations on ion-milled samples of Devonian black shales from Indiana and New York: The petrographic context of multiple pore types. In: *Electron Microscopy of Shale Hydrocarbon Reservoirs* (Camp, W. K., Diaz, E., Wawak, B., eds.). American Association of Petroleum Geologists, Tulsa, OK, U.S.A., 2013, AAPG Memoir **102**, 153–171. http://doi.org/10.1306/13391711M1023589

22. Zhang, H. *Research on Oil Shale Resource Evaluation and Evaluation Methods in Northern of Northeast China*. PhD thesis. Jilin University, China, 2008 (in Chinese).

23. Liu, Z., Yang, H., Dong, Q., Zhu, J., Guo, W. *Oil Shale in China*. Petroleum Industry Press, Beijing, 2009 (in Chinese with English abstract).

24. Feng, Z., Jia, C., Xie, X., Zhang, S., Feng, Z., Cross, T. A. Tectonostratigraphic units and stratigraphic sequences of the nonmarine Songliao basin, northeast China. *Basin Res*., 2010, **22**(1), 79–95. http://doi.org/10.1111/j.1365-2117.2009.00445.x

25. Niu, J., Yu, W., Wang, Z., Luo, Y., Gong, F., Wang, Y. Sedimentary characteristics of oil shale of Qingshankou Formation, lower Cretaceous system in the Songliao Basin, Jilin Province. *Jilin Geology*, 2010, **29**(2), 71–73 (in Chinese with English abstract).

26. Zhang, H., Liu, Z., Shi, J., Meng, Q. Formation characteristics of oil shale in the Lower Cretaceous Dalazi Formation in the Luozigou basin. *Geol. China*, 2007, **34**(1), 86–91 (in Chinese with English abstract).

27. O'Brien, N. R., Slatt, R. M. *Argillaceous Rock Atlas*. Springer-Verlag, 1990. http://doi.org/10.1007/978-1-4612-3422-7

28. Milliken, K. L., Olson, T. Amorphous and crystalline solids as artifacts in SEM images. In: *Imaging Unconventional Reservoir Pore Systems* (Olson, T., ed.). American Association of Petroleum Geologists, Tulsa, OK, U.S.A., 2016, AAPG Memoir **112**, 1–8. https://doi.org/10.1306/13592013M1122252

29. Loucks, R. G., Reed, R. M. Scanning-electron-microscope petrographic evidence for distinguishing organic matter pores associated with depositional organic matter versus migrated organic matter in mudrocks. *GCAGS Journal*, 2014, **3**, 51–60.

30. Wilson, R. D., Schieber, J. The influence of primary and secondary sedimentary features on reservoir quality: Examples from the Geneseo Formation of New York, U.S.A. In: *Imaging Unconventional Reservoir Pore Systems* (Olson, T., ed.). American Association of Petroleum Geologists, Tulsa, OK, U.S.A., 2016, AAPG Memoir **112**, 167–184. https://doi.org/10.1306/13592021M1123697

31. Slatt, R. M., O'Brien, N. R. Pore types in the Barnett and Woodford gas shales: Contribution to understanding gas storage and migration pathways in fine-grained rocks. *AAPG Bull*., 2011, **95**(12), 2017–2030. https://doi.org/10.1306/03301110145

32. Slatt, R. M., O'Brien, N. R. Microfabrics related to porosity development, sedimentary and diagenetic processes, and composition of unconventional resource shale reservoirs as determined by conventional scanning electron microscopy. In: *Electron Microscopy of Shale Hydrocarbon Reservoirs* (Camp, W. K., Diaz, E., Wawak, B., eds.). American Association of Petroleum Geologists, Tulsa, OK, U.S.A., 2013, AAPG Memoir **102**, 37–44. http://doi.org/10.1306/13391703M102441

33. Yu, Y., Liang, W., Bi, J., Geng, Y., Kang, Z., Zhao, Y. Thermophysical experiment and numerical simulation on thermal cracking of oil shale at high temperature.

Chin. J. Rock Mech. Eng., 2015, **34**(6), 1106–1115 (in Chinese with English abstract). https://doi.org/10.13722/j.cnki.jrme.2014.0953

34. Gabova, A., Chekhonin, E., Popov, Y., Savelev, E., Romushkevich, R., Popov, E., Kozlova, E. Experimental investigation of thermal expansion of organic-rich shales. *Int. J. Rock Mech. Min. Sci.*, 2020, **132**, 104398. https://doi.org/10.1016/j.ijrmms.2020.104398

35. Zhu, Y., Liu, K., Zhong, X., Wang, Y., Chen, C., Zhang, H., Pan, D., Zhai, L., Gao, S. Experimental investigation on the anisotropic behaviors induced by bedding planes in mechanical properties of Ma′quan oil shale. *Arab. J. Sci. Eng.*, 2022, **47**, 11385–11403. https://doi.org/10.1007/s13369-021-06027-2

36. Sun, P. *Environmental Dynamics of Organic Accumulation in the Oil Shale Bearing Layers in the Upper Cretaceous, Southeast Songliao Basin (NE China)*. PhD thesis. Jilin University, China, 2013 (in Chinese).

37. Chen, M., Cheng, Y., Li, W. Exploitation and utilization of oil shale in the coal measure strata of the Haishiwan mine, Yaojie coalfield, China. *Oil Shale*, 2015, **32**(4), 335–355. http://doi.org/10.3176/oil.2015.4.04

38. Loucks, R. G., Reed, R. M. Natural microfractures in unconventional shale-oil and shale-gas systems: Real, hypothetical, or wrongly defined? *GCAGS Journal*, 2016, **5**, 64–72.

39. Mastalerz, M., Schieber, J. Effect of ion milling on the perceived maturity of shale samples: Implications for organic petrography and SEM analysis. *Int. J. Coal Geol.*, 2017, **183**, 110–119. http://doi.org/10.1016/j.coal.2017.10.010

40. Schieber, J. Shale microfabrics and pore development – an overview with emphasis on the importance of depositional processes. In: *Gas Shale of the Horn River basin* (Leckie, D. A., Barclay, J. E. eds.). Canadian Society of Petroleum Geologists, Calgary, Canada, 2011, 115–119.

41. Erdman, N., Drenzek, N. Integrated preparation and imaging techniques for the microstructural and geochemical characterization of shale by scanning electron microscopy. In: *Electron Microscopy of Shale Hydrocarbon Reservoirs* (Camp, W. K., Diaz, E., Wawak, B., eds.). American Association of Petroleum Geologists, Tulsa, OK, U.S.A., 2013, AAPG Memoir **102**, 7–14. http://doi.org/10.1306/13391700M1023581

42. Reed, R. M., Loucks, R. G. Low-thermal-maturity (<0.7% VR) mudrock pore systems: Mississippian Barnett Shale, southern Fort Worth Basin. *GCAGS Journal*, 2015, **4**, 15–28.

43. Berner, R. A. Sedimentary pyrite formation: An update. *Geochim. Cosmochim. Acta*, 1984, **48**(4), 605–615. https://doi.org/10.1016/0016-7037(84)90089-9

44. Bernard, S., Bowen, L., Wirth, R., Schreiber, A., Schulz, H-M., Horsfield, B., Aplin, A. C., Mathia, E. J. FIB-SEM and TEM investigations of an organic-rich shale maturation series from the Lower Toarcian Posidonia Shale, Germany: Nanoscale pore system and fluid-rock interactions. In: *Electron Microscopy of Shale Hydrocarbon Reservoirs* (Camp, W. K., Diaz, E., Wawak, B., eds.). American Association of Petroleum Geologists, Tulsa, OK, U.S.A., 2013, AAPG Memoir **102**, 53–66. http://doi.org/10.1306/13391705M1023583